Chemical Science

ROYAL SOCIETY OF CHEMISTRY

EDGE ARTICLE

View Article Online
View Journal | View Issue

Cite this: *Chem. Sci.*, 2021, **12**, 10919

All publication charges for this article have been paid for by the Royal Society of Chemistry

Received 11th March 2021
Accepted 26th June 2021

DOI: 10.1039/d1sc01458g

rsc.li/chemical-science

Correlations between ligand field Δ_o, spin crossover $T_{1/2}$ and redox potential E_{pa} in a family of five dinuclear helicates†

Sandhya Singh and Sally Brooker *

A family of five new bis-bidentate azole–triazole **Rat** ligands (1,3-bis(5-(azole)-4-isobutyl-4*H*-1,2,4-triazol-3-yl)benzene), varying in choice of azole (2-imidazole, 4-imidazole, 1-methyl-4-imidazole, 4-oxazole and 4-thiazole), and the corresponding family of spin-crossover (SCO) and redox active triply bridged dinuclear helicates, $[Fe^{II}_2L_3]^{4+}$, has been prepared and characterised. X-ray crystal structures show all five Fe(II) helicates are low spin at 100 K. Importantly, DOSY NMR confirms the intactness of these SCO-active dinuclear helicates in D_3-MeCN solution, regardless of HS fraction: γ_{HS}(298 K) = 0–0.81. Variable temperature ^{1}H NMR Evans and UV-vis studies reveal that the helicates are SCO-active in MeCN solution. Indeed, the choice of azole in the **Rat** ligand used in $[Fe_2L_3]^{4+}$ tunes: (a) solution SCO $T_{1/2}$ from 247 to 471 K, and (b) reversible redox potential, $E_m(Fe^{II/III})$, from 0.25 to 0.67 V for four helicates, whilst one has an irreversible redox process, E_{pa} = 0.78 V, *vs.* 0.01 M $AgNO_3$/Ag. For the four reversible redox systems, a strong correlation (R^2 = 0.99) is observed between $T_{1/2}$ and E_{pa}. Finally, the analogous Ni(II) helicates have been prepared to obtain Δ_o, establishing: (a) the ligand field strength order of the ligands: 4-imidazole (11 420) ~ 1-methyl-4-imidazole (11 430) < 2-imidazole (11 505) ~ 4-oxazole (11 516) < 4-thiazole (11 804 cm^{-1}), (b) that Δ_o ($[Ni^{II}_2L_3]^{4+}$) strongly correlates (R^2 = 0.87) with $T_{1/2}$ ($[Fe^{II}_2L_3]^{4+}$), and (c) interestingly that Δ_o strongly correlates (R^2 = 0.98) with E_{pa} for the four helicates with reversible redox, so the stronger the ligand field strength, the harder it is to oxidise the Fe(II) to Fe(III).

Introduction

Spin crossover (SCO) is a phenomenon seen in $3d^4$–$3d^7$ octahedral metal complexes when the ligand field is 'just right' so that the application of an external stimulus, including temperature, pressure, light irradiation and guest molecules, causes a reversible switch of spin state, from HS to LS.[1–3] This conversion is accompanied by a pronounced change in colour, volume, mechanical, electrical and magnetic properties of the materials; which gives rise to a multitude of potential applications, in sensing, data storage, actuators, thermometers and display devices.[1,4,5]

The study of self-assembled coordination complex architectures[6] (metallosupramolecular chemistry)[7] has become very popular in the last few decades, not least because of interesting host–guest chemistry, catalysis and sensing ability.[8–10] Discrete polynuclear iron(II) supramolecular architectures are particularly interesting for SCO,[11–13] as (a) intramolecular interactions, electronic and steric, between the metal centres can influence the SCO, amongst other things enhancing the potential for polynary rather than binary information storage through multistep SCO,[4,11] and (b) host–guest interactions can influence the SCO.[14,15] Nevertheless, prior to this study, only 12 ligands (Fig. S1.1, ESI,† **L1–L12**), comprising either azole–pyridine or azole–imine coordinating pockets (Fig. 1), had been employed to form SCO-active dinuclear iron(II) helicates.[11,16] The first example of an SCO-active dinuclear helicate, $[Fe_2\mathbf{L1}_3]^{4+}$ (Fig. S1.1, ESI†) was reported by Williams and co-workers in 1998.[17] Since then this field has been expanded on by various authors, including Hannon,[18] Li,[16,19,20] Kruger and Clérac,[21–23] Sunatsuki,[24,25] and Aromí.[26]

Despite considerable interest in redox properties, especially of iron complexes due to potential relevance to understanding the function of heme-based metalloproteins, in which spin state changes are also crucial,[27–29] studies of SCO and redox in families of complexes are rare:[24,30–35] Drago,[30] Kadish[32,33] and Kuroda-Sowa[31] studied mononuclear complexes, whilst Sunatsuki and co-workers have reported the only examples involving dinuclear iron(II) helicates[24] (or tetranuclear cages[36]). Of these, only the Drago[30] and Kadish[32,33] studies (Fig. S1.2, ESI†) involved

Department of Chemistry, The MacDiarmid Institute for Advanced Materials and Nanotechnology, University of Otago, PO Box 56, Dunedin 9054, New Zealand. E-mail: sbrooker@chemistry.otago.ac.nz

† Electronic supplementary information (ESI) available: Experimental section, crystallographic information, DOSY spectra, NMR spectra, MS spectra, UV-vis spectra, cyclic voltammograms, previously reported SCO-active Fe(II) dinuclear helicates, solid state SCO. CCDC 2061247–2061253, 2090518 and 2090519. For ESI and crystallographic data in CIF or other electronic format see DOI: 10.1039/d1sc01458g

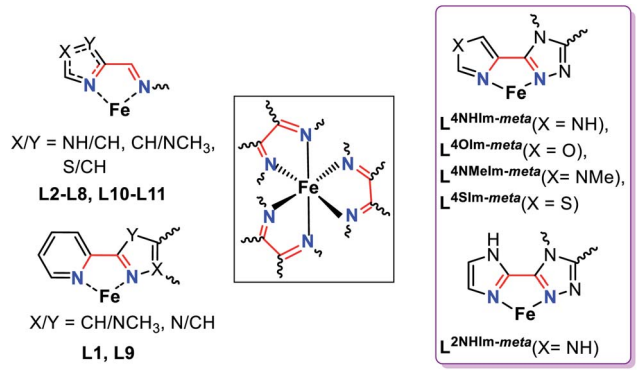

Fig. 1 Summary of the common features (black box) of the bidentate binding pockets in the 12 ligands employed to generate the dinuclear SCO-active triply bridged Fe_2L_3 helicates reported in the literature to date (left, **L1–L12**, see also Fig. S1.1 ESI†),[11] and in the five new ligands presented in this work (right, violet box), $L^{2NHIm\text{-}meta}$, $L^{4NHIm\text{-}meta}$, $L^{4NMeIm\text{-}meta}$, $L^{4OIm\text{-}meta}$ and $L^{4SIm\text{-}meta}$.

solution SCO, which is the most relevant for comparison with the redox potential, also determined in solution.

In the solid state, crystal packing, co-crystallised solvent and intermolecular cooperativity can obscure the electronic modifications imposed by variation of the ligand. In contrast, solution SCO opens the door to investigating the electronic effect arising from ligand modification,[37–40] including from a 'tail',[41–43] as well as the effects of solvent polarity,[44] concentration[41] and pH.[45]

1,2,4-Triazole ligands, which can be substituted at the C^3, N^4 and/or C^5 positions on the triazole ring (Fig. 2), provide an appropriate ligand field strength for generating Fe(II) spin crossover materials.[46–48]

Such ligands have included (Fig. 2): mono- and bis-dentate **Rdpt**,[48] bis-terdentate **PMRT**/**PSRT**[11,49–51] and the related **PMTD**/**PMOD**[52–54] or **TMTD**[55] all of which have been reported in the literature to form SCO active Fe(II) complexes. Recently, we reported that our general synthetic strategy for accessing **Rdpt** ligands[38,56] could be extended to access the first examples of ditopic azine-triazole analogues[57] and of azole–triazole monotopic **Rat** ligands.[58] The first four ditopic azine-triazole ligands prepared, $\mathbf{L}^{n\text{pym}\text{-}meta}$ and $\mathbf{L}^{n\text{pym}\text{-}para}$ (Fig. 2),[57] featured *n*-pyrimidine-triazole binding sites linked by either *meta*- (for helicates) or *para*- (for tetrahedral cages) substituted phenylene linkers. All four of the structurally characterised iron(II) complexes, both helicates and cages, of these first ditopic **Rat** ligand systems were found to be LS.[57] Clearly, the ligand field of these new robust ditopic **Rat** ligands needs to be reduced in order to enable SCO. With this goal in mind, very recently, we reported the first examples of monotopic azole–triazole $\mathbf{L}^{\mathbf{4NMe/SIm}}$ ligands (Fig. 2), which, as expected, imposed a weaker ligand field: $[Fe(\mathbf{L}^{\mathbf{4NMeIm}})_3](BF_4)_2$ is HS whereas $[Fe(\mathbf{L}^{\mathbf{4SIm}})_3](BF_4)_2$ is SCO-active in both the solid state and in MeCN solution.[58]

The focus herein is on the development of a new family of robust yet easily modified ligands for the assembly of SCO-active triply bridged iron(II) dinuclear helicates. Hence the ditopic versions of these weaker fields azole–triazole ligands

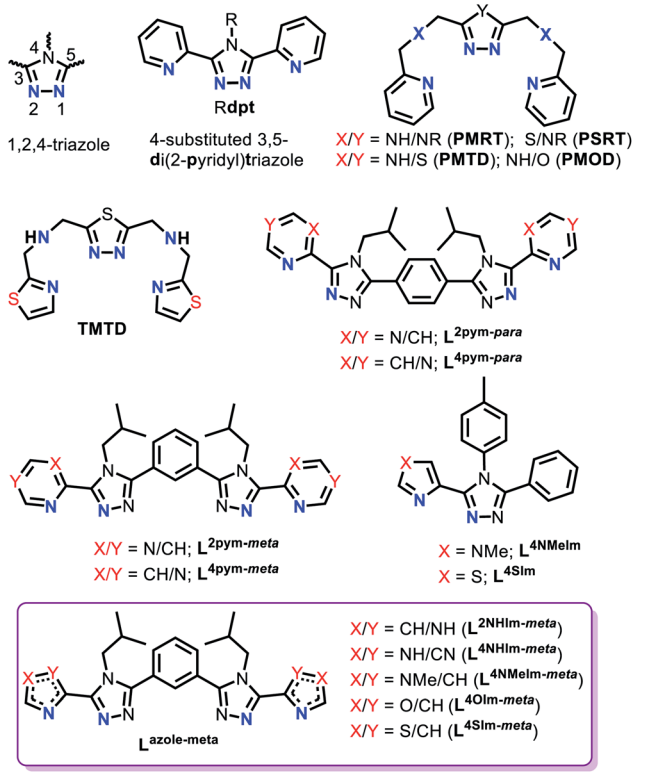

Fig. 2 Generic 1,2,4-triazole numbering (top left), **Rdpt** ligand (top middle), bis-terdentate PMRT/PSRT/PMTD/PMOD/TMTD (top right and second row left), bis-bidentate azine-triazole **Rat** ligands ($L^{2/4pym\text{-}meta/para}$), bidentate azole–triazole **Rat** ligand ($L^{4NMe/SIm}$) and bis-bidentate azole–triazole **Rat** ligands used in this work (bottom; violet box).

($\mathbf{L}^{\mathbf{4NMe/SIm}}$) are prepared, using a *meta*-phenylene linker, to enable access to a new class of SCO-active $[Fe^{II}_2L_3]^{4+}$ dinuclear helicates. Specifically we report the synthesis of five new ditopic **Rat** ligands ($\mathbf{L}^{\mathbf{azole}\text{-}meta}$, Fig. 2, violet box) and the synthesis, structural, spectroscopic, solid and solution spin crossover and redox characterisation of the corresponding triply bridged dinuclear helicates, $[Fe^{II}_2(\mathbf{L}^{\mathbf{azole}\text{-}meta})_3](BF_4)_4$. Furthermore, to determine the ligand field strengths of these new **Rat** ligands, the corresponding Ni(II) helicates are also synthesised, two are structurally characterised and all five are studied by UV-vis spectroscopy.

This study of five helicates provides a rare demonstration of the expected, often said but seldom shown, correlation between the SCO switching temperature ($T_{1/2}$) and the ligand field splitting energy (Δ_o) for a family of complexes. Somewhat less intuitive is that a connection is also established between these spin crossover properties (Δ_o, $T_{1/2}$) and the oxidation potentials (E_{pa}), a combination of properties not often studied together (see above).

Results and discussion

Synthesis

In contrast to the previously published azine-triazole dinuclear helicates featuring a 1,3-phenylene linker ligand, both of which

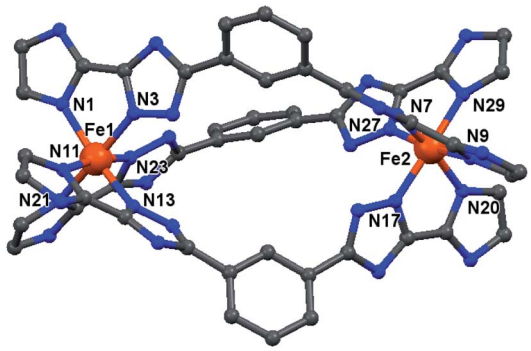

Fig. 3 Molecular structure of the cation of the triply bridged dinuclear helicate, $[Fe_2L^{2NHIm\text{-}meta}{}_3]\cdot 2CH_3CN\cdot$solvent (**1**·solvents). The other four helicates are isostructural with this one (see Fig. S7, ESI†). For clarity, the hydrogen atoms, counter-anions and iso-butyl groups are not shown. Colours: Fe orange; N blue; C grey.

were LS,[57] herein the ligand field induced by the ditopic ligands is reduced. So, whilst the same linker is used, both bidentate ligand binding sites are changed from featuring azine-triazole to azole–triazole binding pockets. The five new ditopic ligands of azole–triazole, 2-imidazole $\mathbf{L}^{2NHIm\text{-}meta}$, 4-imidazole $\mathbf{L}^{4NHIm\text{-}meta}$, 1-methyl-4-imidazole $\mathbf{L}^{4NMeIm\text{-}meta}$, 4-oxazole $\mathbf{L}^{4OIm\text{-}meta}$ and 4-thiazole $\mathbf{L}^{4SIm\text{-}meta}$, were synthesised by refluxing the previously reported ethylated bis-thioamide[57] and appropriate azole carbohydrazide in *n*-butanol for three days, and were obtained as analytically pure powders in 31–56% yield (Scheme S1, ESI†).

Next, the dinuclear Fe(II) helicates were prepared by a one-pot synthesis at room temperature, reacting a 2 : 3 ratio of $Fe(BF_4)_2\cdot 6H_2O$ and the appropriate ligand $\mathbf{L}^{2NHIm\text{-}meta}$ or $\mathbf{L}^{4XIm\text{-}meta}$ (X = NH, NMe, O and S), in acetonitrile except for $\mathbf{L}^{4NHIm\text{-}meta}$ where nitromethane was used. In addition, nitromethane was used to obtain a solvatomorph of $[Fe_2(\mathbf{L}^{4OIm\text{-}meta})_3](BF_4)_4$ (crystal structure determined at 100 and 253 K, see below). Similarly, the five $[Ni_2L_3](BF_4)_4$ helicates were obtained, in order to determine Δ_o from the UV-vis spectra, by using $Ni(BF_4)_2\cdot 6H_2O$ and acetonitrile as the solvent.

All five $[Fe^{II}_2L_3](BF_4)_4$ complexes were obtained as single crystals suitable for X-ray crystallography (Fig. S4, ESI†), by slow vapour diffusion of diethyl ether into the reaction solutions: dark orange blocks of $[Fe_2(\mathbf{L}^{2NHIm\text{-}meta})_3](BF_4)_4\cdot 2CH_3CN\cdot$solvent (**1**·solvents), light brown plates of $[Fe_2(\mathbf{L}^{4NHIm\text{-}meta})_3](BF_4)_4\cdot$solvent (**2**·solvent), light orange-yellow irregular blocks of $[Fe_2(\mathbf{L}^{4NMeIm\text{-}meta})_3](BF_4)_4\cdot 6CH_3CN\cdot C_4H_{10}O$ (**3**·$6CH_3CN\cdot C_4H_{10}O$), violet-pink needles of $[Fe_2(\mathbf{L}^{4OIm\text{-}meta})_3](BF_4)_4\cdot 6CH_3CN\cdot$solvent (**4**·solvents), and dark orange blocks of $[Fe_2(\mathbf{L}^{4SIm\text{-}meta})_3](BF_4)_4\cdot$solvent (**5**·solvents). After air drying, compounds **1**–**5** were obtained, as analytically pure powders (Fig. S6, ESI†), as the following solvatomorphs, all hydrates, in 30–87% yield: **1**·$4H_2O$ (orange, 73%), **2**·$6H_2O$ (brown, 30%), **3**·$5H_2O$ (orange, 87%), **4**·$6H_2O$ (grey, 37%) and **5**·$2.5H_2O$ (orange, 87%).

In the same way, the analogous dinuclear Ni(II) helicates were prepared and isolated by vapour diffusion of diethyl ether into the MeCN reaction solutions. After air drying, $\mathbf{1}^{Ni}$–$\mathbf{5}^{Ni}$ were obtained, as analytically pure pale violet/pink powders (Fig. S9, ESI†), as the following solvatomorphs, all hydrates, in 50–96% yield: $\mathbf{1}^{Ni}\cdot 6H_2O$ (62%), $\mathbf{2}^{Ni}\cdot 4H_2O$ (50%), $\mathbf{3}^{Ni}\cdot 5H_2O$ (92%), $\mathbf{4}^{Ni}\cdot 2.5H_2O$ (62%) and $\mathbf{5}^{Ni}\cdot 3H_2O$ (96%).

Crystal structure descriptions

Single crystal X-ray data for all five of the Fe(II) dinuclear helicates were collected at 100 K. In all but one case data collection at higher temperatures was not possible due to loss of crystallinity: the exception was **4**·$5.5NO_2CH_3$, which on warming to 253 K appeared to lose about half a molecule of nitromethane of crystallisation, becoming **4**·$5NO_2CH_3$ for which data was able to be collected. Modelling of the disorder of some iso-butyl groups, and of some anions, is detailed in ESI.† Due to solvent disorder that could not be modelled satisfactorily, the SQUEEZE[59] routine in PLATON[59] was applied to five of the datasets: **1**·solvents, **2**·solvents, **4**·solvents **4**·$5NO_2CH_3$ and **5**·solvents, (see ESI† for details).

All of the dinuclear helicates (Fig. 3) crystallised in centrosymmetric space groups: **1**·solvents (triclinic $P\bar{1}$), **2**·solvents (orthorhombic *Pbca*), **3**·$6CH_3CN\cdot C_4H_{10}O$ (triclinic $P\bar{1}$), **4**·solvents (triclinic $P\bar{1}$), **4**·$5.5NO_2CH_3$ (100 K, triclinic $P\bar{1}$), **4**·$5NO_2CH_3$ (253 K, triclinic $P\bar{1}$) and **5**·solvents (monoclinic *C*2/*c*). The entire helicate, $[Fe_2L_3](BF_4)_4\cdot$solvents, was present in the asymmetric unit for all of them, except **5**·solvents in which half of the helicate, $[FeL_{1.5}](BF_4)_2\cdot$solvents, was present with the other half generated by a 2-fold axis.

In all cases, the formation of the desired triply bridged dinuclear helicate is confirmed. The N_6 coordination sphere forms a distorted octahedral geometry at Fe(II) centre, and comprises the pair of donors from one end of each of the three

Table 1 Selected geometric parameters of dinuclear Fe^{II} and Ni^{II} (green rows) helicates at 100 K, except for **4**·$5NO_2CH_3$ at 253 K. HS Fe(II) in bold text, octahedral Ni(II) in blue text

Complexes	Space group	⟨Fe–N⟩ (Å)	Σ°	Spin state	M···M (Å)
1·solvents	$P\bar{1}$	1.967, 1.962	60.9, 59.7	LS, LS	10.0361(6)
$\mathbf{1}^{Ni}$·solvents	$P2_1/n$	2.097, 2.076	75.2, 70.2	$S = 1$	10.313(1)
2·solvents	*Pbca*	1.972, 1.971	58.7, 57.8	LS, LS	10.1619(9)
$\mathbf{2}^{Ni}$·solvents	*Ibca*	2.083	69.7	$S = 1$	10.3891(8)
3·$6CH_3CN\cdot C_4H_{10}O$	$P\bar{1}$	1.980, 1.980	62.0, 61.5	LS, LS	10.3227(7)
4·solvents	$P\bar{1}$	1.973, 1.964	57.0, 56.8	LS, LS	10.018(1)
4·$5.5NO_2CH_3$	$P\bar{1}$	1.967, **2.058**	62.0, **77.2**	LS, mixLS/**HS**	10.1554(7)
4·$5NO_2CH_3$ (253 K)	$P\bar{1}$	1.980, **2.181**	63.0, **95.3**	LS, **HS**	10.2281(9)
5·solvents	*C*2/*c*	1.953	57.0	LS	9.9711(9)

distinct bis-bidentate azole–triazole **Rat** ligands (Fig. 3 and S7, ESI†).

Excluding the nitromethane solvatomorphs of **4** (see later), at 100 K all of the Fe–$N_{azole/triazole}$ distances fall in the range of 1.934–2.000 Å (Table S1, ESI†), which is consistent with LS Fe(II). The octahedral distortion parameters (sum of deviations of the 12 *cis* angles from 90°) of the Fe(II) centres in **1–5** lie in a narrow range, 56.8–62.0° (Tables 1 and S1, ESI†) that is close to those seen for the LS azine-triazole Fe(II) dinuclear helicates $[Fe_2\text{-}\mathbf{L}^{2pym\text{-}meta}{}_3](BF_4)_4$ (56.7°) and $[Fe_2\mathbf{L}^{4pym\text{-}meta}{}_3](BF_4)_4$ (60.3°), and falls in the range seen for all of the SCO-active helicates reported in the literature (51–70°).[11,57] The intrahelicate Fe···Fe distances in **1–5** lie between 9.971–10.323 Å (Table 1), which falls in the range of 9–12 Å reported for seven of the literature examples SCO-active Fe(II) helicates[17,19–21,26,60] (exception ~ 4 Å (**L7**/**L8**),[24,25] ~15 Å (**L10**/**L11**)[23] and 19 Å (**L12**),[16] Fig. S1.1, ESI†).

Only for the nitromethane solvates of the oxazole–triazole helicate could datasets be collected at two temperatures: $\mathbf{4}\cdot 5.5NO_2CH_3$ at 100 K and $\mathbf{4}\cdot 5NO_2CH_3$ at 253 K (some nitromethane lost on warming). The resulting parameters (Tables 1 and S1†) are consistent with the helicate being in a [LS–mixedLS/HS] state at 100 K and a [LS–HS] state at 253 K (Fig. 4, Table 1). At 100 K, the [LS–mixedLS/HS] state is proposed as the average Fe–N bond distances and $\sum^\circ$ are 1.967 Å and 62° for Fe1 (LS) and 2.058 Å and 77° for Fe2 (mixedLS/HS). The $\sum^\circ$ value for mixedLS/HS Fe2 is higher than is usual for LS Fe(II) in Fe_2L_3 helicates (51–70°),[11] and is close to that seen for mixedLS/HS $[Fe^{II}_2(\mathbf{L2})_3](BF_4)_4\cdot 2MeCN$ ($\sum^\circ$ = 76°).[11,60] The average intraligand N_{azole}–Fe–$N_{triazole}$ angles are 80.7 (LS) and 78.5°(mixedLS/HS). At 253 K, $\mathbf{4}\cdot 5NO_2CH_3$ is in the [LS–HS] state as the SCO at Fe2 is now complete, whilst Fe1 remains LS (Table 1), as shown by the Fe–N and $\sum^\circ$ values 1.980 Å and 63.0° for Fe1 *versus* 2.181 Å and 95.3° for Fe2 (Table 1 and Fig. 4). On conversion to LS–HS, the average intraligand N_{azole}–Fe–$N_{triazole}$ angles are 80.3 (LS) and 75.8° (HS, a reduction of ~3°; similar to 75.7° seen for the mononuclear HS 1-methyl-4-imidazole complex[58] $[FeL_3](BF_4)_2$, Table S1, ESI†). The Fe···Fe distance expands from 10.1554(7) [LS-mixLS/HS] to 10.2281(9) Å [LS–HS].

The structures of two of the dinuclear Ni(II) helicate analogues, those of the 2- and 4-NH imidazole ligands $\mathbf{L}^{2NHIm\text{-}meta}$ and $\mathbf{L}^{4NHIm\text{-}meta}$, were also obtained at 100 K. The Ni–N distances (2.069–2.103 Å)[61] and octahedral distortion values ($\sum^\circ$ = 69.7–75.2°) are in between those expected for HS and LS Fe(II). In both cases, the average intraligand N_{azole}–Fe–$N_{triazole}$ angle (78.3/78.7 and 78.8°, Table S1, ESI†) falls in between those seen for HS and LS Fe(II), and an increase of 2–3% in M···M distance was observed on LS Fe(II) → Ni(II) (Table 1).

ESI-MS and ^{1}H DOSY NMR spectra

The ESI-MS and ^{1}H DOSY NMR spectra both showed the dinuclear helicates **1–5** are intact in acetonitrile solution (Fig. S67–S95 and S62–S66, ESI†), confirming the robust nature of these $[Fe_2L_3]^{4+}$ helicates. Specifically, the ESI-MS spectra showed the presence of $[Fe_2L_3]^{4+}$, $[Fe_2L_3](X)^{3+}$ and $[Fe_2L_3](X)_2{}^{2+}$ (X = F or BF_4) species.

Diffusion ordered ^{1}H NMR spectroscopy (DOSY) was initially developed for use in characterising aggregates such as micelles, protein fragments and coordination polymers.[62–64] Further development led to its widespread use in determining the molecular weights[65] and size of polymers[65,66] and to study molecular interaction between frustrated Lewis acid–base pairs in solution.[67,68] Indeed it is now the 'go to' technique in supramolecular chemistry for determining the molecular weight and hence *n* for large diamagnetic self-assembled architectures, as is exemplified by the huge Pd_nL_{2n} (n = 12, 24 and 30) cages assembled by Fujita and co-workers.[64,69–71]

Maury, Giraud and co-workers were the first to use DOSY to characterise paramagnetic lanthanide complexes.[72] Later on, Byers and co-workers successfully extended the use of DOSY to the determination of molecular weights of paramagnetic 3d transition metal complexes.[73] Building on that report, DOSY is used here to analyse the intactness of this family of five paramagnetic dinuclear helicates, **1–5**, in MeCN solution at 298 K. The ^{1}H DOSY signals

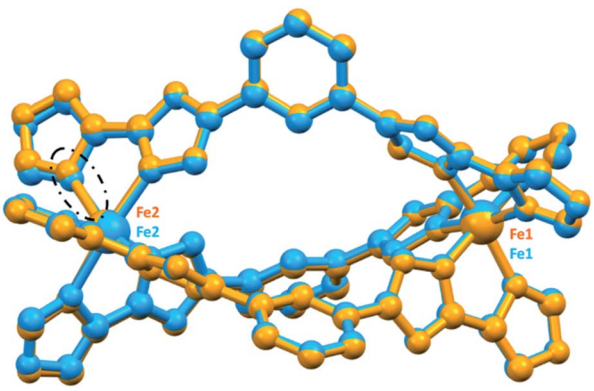

Fig. 4 Overlay of the structures (all atoms fitted) of the nitromethane solvates, [LS–mixedLS/HS] $\mathbf{4}\cdot 5.5NO_2CH_3$ at 100 K (blue) and [LS–HS] $\mathbf{4}\cdot 5NO_2CH_3$ at 253 K (orange), emphasising the lengthening of the Fe2–N bond (in the black dashed ellipse) and increased distortion around the Fe2 > Fe1.

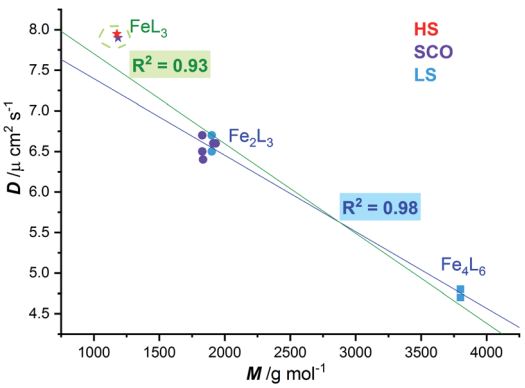

Fig. 5 Correlation (dark blue line, $R^2 = 0.98$) of diffusion coefficient (D) with molecular weight (M) observed at 298 K for LS $Fe^{II}_2L_3$ helicates (blue circles) and $Fe^{II}_4L_6$ cages (blue squares),[57] and the SCO-active $Fe^{II}_2L_3$ helicates reported here (violet circles). When the two mononuclear $Fe^{II}L_3$ complexes, one HS and one SCO, are included in the fit, the R^2 only drops to 0.93 (green line), despite them not being members of the $Fe_{2n}L_{3n}$ family.

revealed the same diffusion coefficients ($D \sim 6 \times 10^{-6}$ cm^2 s^{-1}; range 6.4–6.7 $\times$ 10^{-6} cm^2 s^{-1}) for all five dinuclear helicates, regardless of the variation in HS fraction at 298 K (from 0 to 0.80, see next section). This confirms the ESI-MS finding that all five helicates are robust in MeCN solution.

Regardless of the spin state at 298 K, a plot of the diffusion coefficients *vs.* molecular weight (Fig. 5), for these five SCO active dinuclear helicates (**1–5**), along with the previously reported LS helicates $[Fe_2(\mathbf{L}^{2/4pym\text{-}meta})_3](BF_4)_4$ and cages $[Fe_4(\mathbf{L}^{2/4pym\text{-}para})_3](BF_4)_8$,[57] gave an excellent correlation ($R^2 = 0.98$, dark blue line). The results for the pair of mononuclear HS and SCO $[Fe(\mathbf{L}^{4NMe/SIm})_3](BF_4)_2$ complexes are also shown (stars, Fig. 5) for completeness. Whilst these are not expected to lie on this correlation line (dark blue line, Fig. 5), as they are not members of the $Fe_{2n}L_{3n}$ family, including them in the correlation only drops the R^2 to 0.93 (green line, Fig. 5).

Variable temperature ^{1}H NMR Evans method

The magnetic response in solution is not affected by crystal packing effects, intermolecular cooperativity or co-crystallised solvents. The absence of all of these effects in the solution enables the effect of ligand modifications on the ligand field strength imposed on the Fe(II) centres to be clearly seen.[39,74,75] Hence, the spin state of the five new dinuclear helicates **1–5** is monitored in acetonitrile solution at variable temperatures using both the ^{1}H NMR Evans method and by UV-vis spectroscopy (discussed in this and the following sections).

The Evans method was used to determine magnetic susceptibility of dinuclear helicates **1–5** in accurately prepared, approximately 6 mM CD_3CN solution in the temperature range 243–343 K (Fig. S36–S40, ESI†), expected error associated with $T_{1/2}$ is 5–10% (Fig. S31–S35, ESI†). Four of the complexes, **1**·4H$_2$O, **2**·6H$_2$O, **3**·5H$_2$O and **4**·6H$_2$O, undergo partial SCO whereas the fifth complex, **5**·2.5H$_2$O, remains mostly LS (Fig. 6). Fitting the data to the regular solution model,[76] as a one-step SCO (Fig. 6), gave $T_{1/2}$ values of 331 K (**1**·4H$_2$O), 267 K (**2**·6H$_2$O), 247 K (**3**·5H$_2$O), 249 K (**4**·6H$_2$O) and 471 K (**5**·2.5H$_2$O).

For **1**·4H$_2$O, the $\chi_m T$ value (per Fe^{II} ion) increased from 0.37 to 1.91 cm^3 K mol^{-1} on increasing the temperature from 243 to 333 K (Fig. 6, black), which corresponds to an increase in high spin fraction (γ_{HS}) of 0.1 $\rightarrow$ 0.5, whilst for **2**·6H$_2$O the $\chi_m T$ (per Fe^{II} ion) increased from 1.38 to 2.67 cm^3 K mol^{-1} (Fig. 6, red), which corresponds to an increase in γ_{HS} of 0.37 $\rightarrow$ 0.72. The $T_{1/2}$ of the 2-imidazole helicate **1**·4H$_2$O ($T_{1/2}$ = 331 K) is higher than that of the 4-imidazole helicate **2**·6H$_2$O ($T_{1/2}$ = 267 K) which implies that the ligand field imposed by 2-imidazole is stronger than that imposed by 4-imidazole, consistent with the Kruger's **L10** and **L11** dinuclear helicates (Fig. S1.1, ESI†),[23] and with the relative ligand field strengths calculated from the UV-vis of analogous Ni(II) helicates of $\mathbf{L}^{2NHIm\text{-}meta}$ and $\mathbf{L}^{4NHIm\text{-}meta}$ (see later). The $\chi_m T$ value (per Fe^{II} ion) for **3**·5H$_2$O at 243 K of 1.73 cm^3 K mol^{-1} increased to 3.36 cm^3 K mol^{-1} at 343 K (Fig. 6, blue), which corresponds to an increase in γ_{HS} of 0.47 $\rightarrow$ 0.91. The only difference between the ligands in **2**·6H$_2$O ($T_{1/2}$ = 267 K) and those in **3** ($T_{1/2}$ = 247 K) is the methylation of the non-coordinated 4-imidazole NH to give the NMe, but this change significantly decreases the ligand field imposed in **3**·5H$_2$O. Halcrow previously commented on the hydrogen bonding by 4-imidazole, increasing the acidity of the –NH hydrogen which increases the electron-density of the coordinated N, strengthening the σ bond donation in the N–Fe bond and favouring the LS state, relative to the methylated analogue,[40] and the present findings are consistent with this.

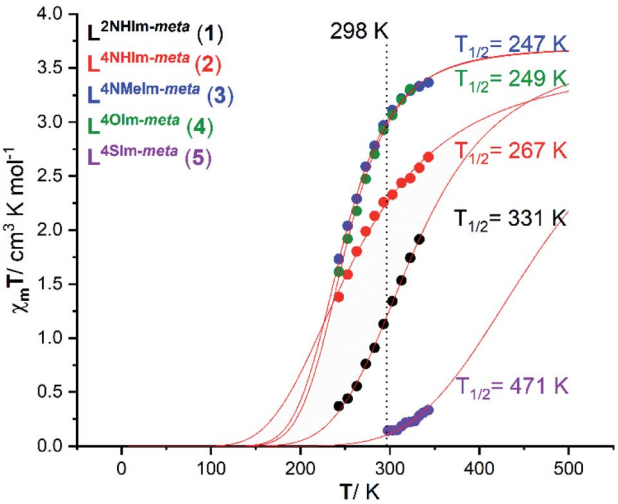

Fig. 6 Plot of $\chi_m T$ *vs.* *T* for **1**·4H$_2$O (black), **2**·6H$_2$O (red), **3**·5H$_2$O (blue), **4**·6H$_2$O (green) and **5**·2.5H$_2$O (purple) in CD_3CN solution, as determined by Evans method.[77,78] The curves correspond to the best fit found for a complete one-step SCO using the regular solution model (see ESI† for details).[51,76]

Almost identical behaviour to the 1-methyl-4-imidazole helicate **3**·5H$_2$O ($T_{1/2}$ = 247 K) is observed for the 4-oxazole helicate **4**·6H$_2$O (Fig. 6, green). The latter, **4**·6H$_2$O, had a $\chi_m T$ value (per Fe^{II} ion) at 243 K of 1.61 which increased to 3.30 cm^3 K mol^{-1} at 323 K ($T_{1/2}$ = 249 K), which corresponds to an increase in γ_{HS} of 0.44 $\rightarrow$ 0.89.

In contrast to **1–4**, the 4-thiazole helicate **5**·2.5H$_2$O remains practically diamagnetic, with a $\chi_m T$ = 0.14 cm^3 K mol^{-1} at 298 K which increased to 0.33 cm^3 K mol^{-1} at 343 K, which corresponds to an increase in γ_{HS} from 0.04 $\rightarrow$ 0.09. Measurements at higher temperatures were not possible due to the boiling point of CD_3CN (354 K). The fit to the regular solution model gave $T_{1/2}$ = 471 K (which should be taken with caution as it involves extrapolation of the data), which is consistent with the 4-thiazole ligand imposing the strongest field ligand of the five studied herein (see later).

In summary, the observed $T_{1/2}$ values for **1–5**, in increasing order, is as follows (**3** ~ **4** < **2** < **1** < **5**):

$$\mathbf{L}^{4NMeIm\text{-}meta}\ (247) \sim \mathbf{L}^{4OIm\text{-}meta}\ (249) < \mathbf{L}^{4NHIm\text{-}meta}\ (267) < \mathbf{L}^{2NHIm\text{-}meta}\ (331) < \mathbf{L}^{4SIm\text{-}meta}\ (471\ \text{K})$$

Variable temperature solid state magnetic measurements

In contrast to the above, the magnetic studies of the hydrates of these five helicates in the solid state (Fig. S142–146, ESI†)

showed that both the 2NH-imidazole $\mathbf{L}^{\mathbf{2NHIm}\text{-}meta}$ ($\mathbf{1}\cdot 4H_2O$) and 4-thiazole $\mathbf{L}^{\mathbf{4SIm}\text{-}meta}$ ($\mathbf{5}\cdot 2.5H_2O$) based helicates remain mostly LS, with only small fractions of HS above 300 K. The other three helicates, of the 4NH-imidazole $\mathbf{L}^{\mathbf{4NHIm}\text{-}meta}$ ($\mathbf{2}\cdot 6H_2O$), 4-oxazole $\mathbf{L}^{\mathbf{4OIm}\text{-}meta}$ ($\mathbf{4}\cdot 6H_2O$) ligands and 4NMe-imidazole $\mathbf{L}^{\mathbf{4NMeIm}\text{-}meta}$ ($\mathbf{3}\cdot 5H_2O$), undergo incomplete SCO with $T_{1/2}$ values of 200, 230 and 280 K, respectively. These $T_{1/2}$ values place the helicates in a different order, $\mathbf{2}\cdot 6H_2O$ < $\mathbf{3}\cdot 5H_2O$ < $\mathbf{4}\cdot 6H_2O$ < $\mathbf{1}\cdot 4H_2O$ ~$\mathbf{5}\cdot 2.5H_2O$, from the above solution studies, once again demonstrating the often confounding impact of lattice solvent and crystal packing on solid state SCO.

Variable temperature UV-vis studies

UV-vis spectra of **1–5** in acetonitrile solution were obtained at variable temperatures in our cryostat, in 10 K steps from 253 to 303 K, to probe the SCO of each of these helicates (Fig. S41–S51, ESI†), and the data compared with the Evans NMR method data (Tables S9–S11, ESI†). The spectra of the four complexes at 253 K are shown in Fig. 7, with the Laporte forbidden, spin allowed d–d transition of the LS Fe(II) centres, $^1A_{1g} \rightarrow {}^1T_{1g}$, clearly seen at approximately 540 nm in the case of $\mathbf{2}\cdot 6H_2O$, $\mathbf{3}\cdot 5H_2O$ and $\mathbf{4}\cdot 6H_2O$, and at 524 nm for $\mathbf{5}\cdot 2.5H_2O$. In contrast, in the case of $\mathbf{1}\cdot 4H_2O$, a charge transfer transition (Fig. S41, ESI†), at room temperature 446 nm ($\varepsilon = 5646$ L mol^{-1} cm^{-1}) obscured this d–d transition, so this charge transfer transition was monitored instead, as such bands have also been used by others to monitor SCO.[79]

For the four complexes that undergo a significant amount of SCO in this temperature range (all but $\mathbf{5}\cdot 2.5H_2O$, see later), the ε values obtained from the variable temperature UV-vis study were plotted against the γ_{HS} values from the Evans method NMR analysis, enabling a calibration line to be fitted, and in turn conversion of the ε values into γ_{HS} values (Table S11, ESI†). In turn, this enables the calculation of an estimated value for the true ε value for the fully LS complexes, ε_{max} (Fig. S52 and S54, ESI†). With that value in hand, the ε *vs.* T values can be fitted with the regular solution model,[51,76] to a full SCO from [LS–LS] → [HS–HS], to obtain the $T_{1/2}$ values (Fig. S53 and S55, ESI†).

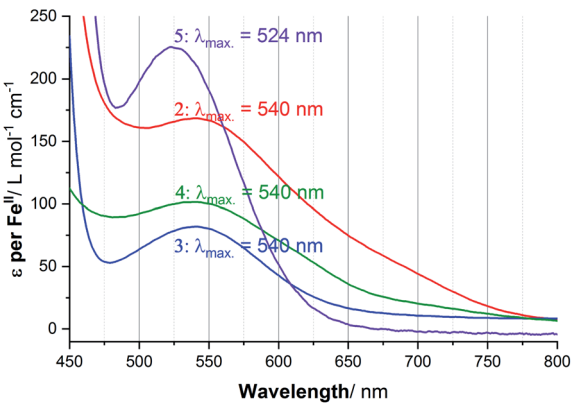

Fig. 7 UV-vis spectra at 253 K in acetonitrile solution, highlighting the d–d transition, of $\mathbf{2}\cdot 6H_2O$ ($\lambda_{max} = 540$ nm, $\varepsilon = 174$, red), $\mathbf{3}\cdot 5H_2O$ ($\lambda_{max} = 540$ nm, $\varepsilon = 82$, blue), $\mathbf{4}\cdot 6H_2O$ ($\lambda_{max} = 540$ nm, $\varepsilon = 102$, green) and $\mathbf{5}\cdot 2.5H_2O$ ($\varepsilon = 225$, purple), and lack of a distinct d–d transition for $\mathbf{1}\cdot 4H_2O$ (charge transfer band at 446 nm, $e = 5642$). Note: ε is calculated per Fe^{II} ion.

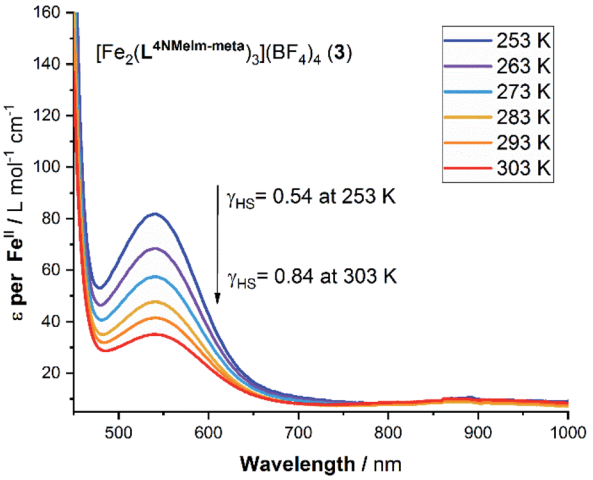

Fig. 8 Variable temperature UV-vis spectroscopy study of a 2 mM acetonitrile solution of $\mathbf{3}\cdot 5H_2O$. Note: ε is calculated per mole of Fe^{II}.

Considering the spectrum of 0.032 mM of the 2-imidazole complex $\mathbf{1}\cdot 4H_2O$ in acetonitrile, the charge transfer transition band observed at $\lambda_{max} = 446$ nm with extinction coefficient per Fe^{II} ion of 8597 L mol^{-1} cm^{-1} at 253 K (Fig. S42, ESI†) which dropped to 4863 at 303 K, with $T_{1/2} = 306$ K. In contrast, d–d transition band were seen at $\lambda_{max} = 524$ to 540 nm for the other four complexes (Fig. 7). In the case of the 4-imidazole complex $\mathbf{2}\cdot 6H_2O$, the temperature dependence band at 540 nm, ε (per Fe^{II} ion) dropped from 174 → 107 L mol^{-1} cm^{-1} while heating from 253 K to 303 K, respectively, $T_{1/2} = 267$ K (Fig. S44, ESI†). Similarly, for 1-methyl-4-imidazole complex $\mathbf{3}\cdot 5H_2O$ d–d band at 540 nm ε value per Fe^{II} ion vary from 82 to 35 L mol^{-1} cm^{-1} ($T_{1/2}$ of 251 K) (Fig. 8). Further, monitoring of the 540 nm band of 4-oxazole complex ($\mathbf{4}\cdot 6H_2O$), the ε value (per Fe^{II} ion) of 102 L mol^{-1} cm^{-1} at 253 K decreased to 58 L mol^{-1} cm^{-1} at 303 K, $T_{1/2} = 265$ K (Fig. S47, ESI†).

In the 4-thiazole helicate $\mathbf{5}\cdot 2.5H_2O$ (Fig. 7), the d–d transition occurs at slightly higher energy (524 nm) than for **2–4**, and only a small change is observed in the ε value. The apparent ε (per Fe^{II} ion) decreased from 225 to 198 L mol^{-1} cm^{-1} on warming from 253 K to 303 K (Fig. S51, ESI†). As this temperature range does not overlap with that of the Evans method data in the region where a non-zero Δf and hence $\chi_m T$ value was observed, this could not be analysed in the same way as for the other four complexes.

Ligand field strengths of $\mathbf{L}^{\mathbf{azole}\text{-}meta}$ ligands

The analogous Ni(II) helicates, $\mathbf{1}^{\mathbf{Ni}}$–$\mathbf{5}^{\mathbf{Ni}}$, have been prepared and characterised (see the experimental section, ESI-MS in Fig. S96–S115† and crystal structures of two in Fig. S10, ESI† for details) as analysis of the UV-vis spectra of them (Fig. S56, ESI†) enables the ligand field splitting energy, Δ_o ($10Dq$), to be obtained, and compared with the $T_{1/2}$ values observed for the Fe(II) helicates.

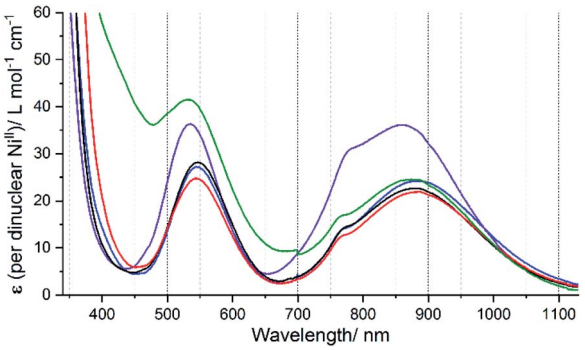

Fig. 9 UV-vis spectra of precisely known but approximately 3 mM of dinuclear Ni(II) helicates in acetonitrile solution; $\mathbf{1}^{Ni}\cdot 6H_2O$ (black), $\mathbf{2}^{Ni}\cdot 4H_2O$ (red), $\mathbf{3}^{Ni}\cdot 5H_2O$ (blue) and $\mathbf{4}^{Ni}\cdot 2.5H_2O$ (green), and $\mathbf{5}^{Ni}\cdot 3H_2O$ (purple). NB. Grating change was at 700 nm.

Octahedral Ni^{2+} (d^8) has a $^3A_{2g}$ ground state, which gives rise to three spin allowed d–d transitions,[80] from highest to lowest energy: $^3A_{2g} \rightarrow {}^3T_{1g}$ (P) ≈ 400–310 nm, $^3A_{2g} \rightarrow {}^3T_{1g}$ (F) ≈ 715–550 nm, and $^3A_{2g} \rightarrow {}^3T_{2g}$ (F) ≈ 1000–800 nm (near IR). This last band corresponds to Δ_o, but it is often weak and broad, and sometimes the spin forbidden $^3A_{2g} \rightarrow {}^1E_g$ transition (which gains some intensity through spin–orbit coupling with $^3T_{2g}$) can be seen as a shoulder on this band, further complicating the analysis.[80,81] Indeed, when Δ_o is close to 12 000 cm^{-1}, as it is herein, mixing of these two bands, $^3A_{2g} \rightarrow {}^3T_{2g}$ (F) and $^3A_{2g} \rightarrow {}^1E_g$, becomes more significant and it is not possible to correctly analyse them. To deal with this issue, Hart, Boeyens and Hancock[81] developed an empirical relationship:

$$10Dq \text{ (corrected)} = 10630 + 1370\varepsilon_1/\varepsilon_2$$

where $\varepsilon_1/\varepsilon_2$ is the ratio of the extinction coefficients of the lower to higher wavelength components of this near IR band.

Using this equation on the ratio of the extinction coefficients corresponding to the shoulder (ε_1)/peak (ε_2) in the near IR band observed in each of the spectra of $\mathbf{1}^{Ni}$–$\mathbf{5}^{Ni}$ (Fig. 9), the "corrected $10Dq$" values, $\Delta_{o(corr.)}$, have been determined for these five helicates (Table S12, ESI†).

In summary, the resulting $\Delta_{o(corr.)}$ values, in order of increasing ligand field strength, as follows (cm^{-1}):

$$\mathbf{L}^{4NHIm\text{-}meta}\ (11\,420) \sim \mathbf{L}^{4NHIm\text{-}meta}\ (11\,430) < \mathbf{L}^{2NHIm\text{-}meta}\ (11\,505) \sim \mathbf{L}^{4OIm\text{-}meta}\ (11\,516) < \mathbf{L}^{4SIm\text{-}meta}\ (11\,804)$$

This analysis of the UV-vis spectra of the Ni(II) helicates shows that the effect of changing from –NH, –NMe and –O in the non-coordinating position of the azole moiety in the ligand leads to relatively minor changes in the field strength, whereas changing to –S provides a significant increase in the ligand field strength. The ligand field strengths of these five ligands $\Delta_{o(corr.)}$ are not entirely consistent with the $T_{1/2}$ values of the corresponding Fe(II) complexes, but despite this there is a good linear correlation ($R^2 = 0.87$) between them (Fig. 10).

Electrochemical studies

The magnetic response of **1–5** varied considerably with small modifications to the ligand strands, clearly reflecting the effect of changing the heteroatom present in the azole rings of these **Rat** ligands on the Fe(II) centres, we also expected to see tuning of the $Fe^{II/III}$ redox potentials.

Cyclic voltammetry was performed on 1 mM MeCN solutions of **1–5**, *vs.* 0.01 M $Ag/AgNO_3$. These solutions also contained 0.1 M $TBAClO_4$, except in the case of 4-thiazole helicate $\mathbf{5}\cdot 2.5H_2O$, which was insoluble in 0.1 M $TBAClO_4$ but was

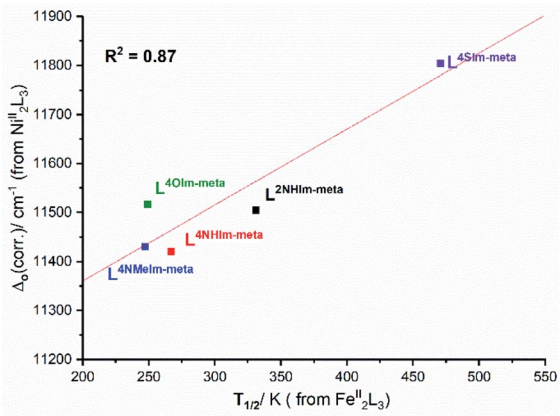

Fig. 10 Good correlation ($R^2 = 0.87$) of $\Delta_{o(corr.)}$ obtained from UV-vis studies of the Ni(II) helicates with solution $T_{1/2}$ obtained for the analogous Fe(II) helicates.

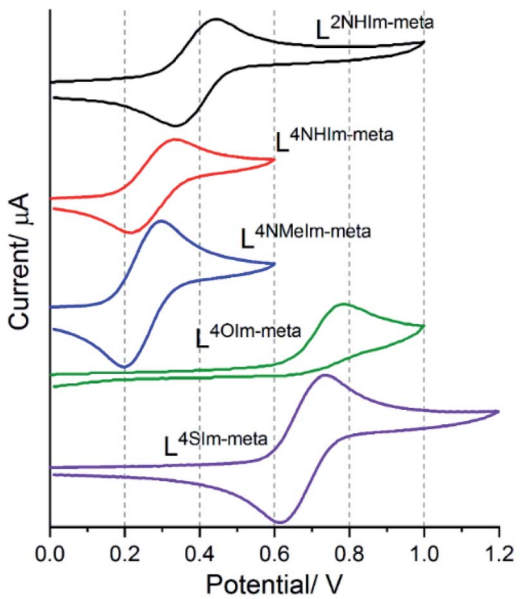

Fig. 11 Cyclic voltammograms of 1 mM solutions (top to bottom): $[Fe^{II}_2(L^{2NHIm\text{-}meta})_3](BF_4)_4\cdot 4H_2O$ ($\mathbf{1}\cdot 4H_2O$, black), $[Fe^{II}_2(L^{4NHIm\text{-}meta})_3](BF_4)_4\cdot 6H_2O$ ($\mathbf{2}\cdot 6H_2O$, red), $[Fe^{II}_2(L^{4NMeIm\text{-}meta})_3](BF_4)_4\cdot 5H_2O$ ($\mathbf{3}\cdot 5H_2O$, blue) and $[Fe^{II}_2(L^{4OIm\text{-}meta})_3](BF_4)_4\cdot 6H_2O$ ($\mathbf{4}\cdot 6H_2O$, green), in MeCN (0.1 mol L^{-1} $TBAClO_4$) and $[Fe^{II}_2(L^{4SIm\text{-}meta})_3](BF_4)_4\cdot 2.5H_2O$ ($\mathbf{5}\cdot 2.5H_2O$, purple) (0.1 mol L^{-1} $TBAPF_6$) *versus* 0.01 mol L^{-1} $Ag/AgNO_3$ at 200 mV s^{-1}.

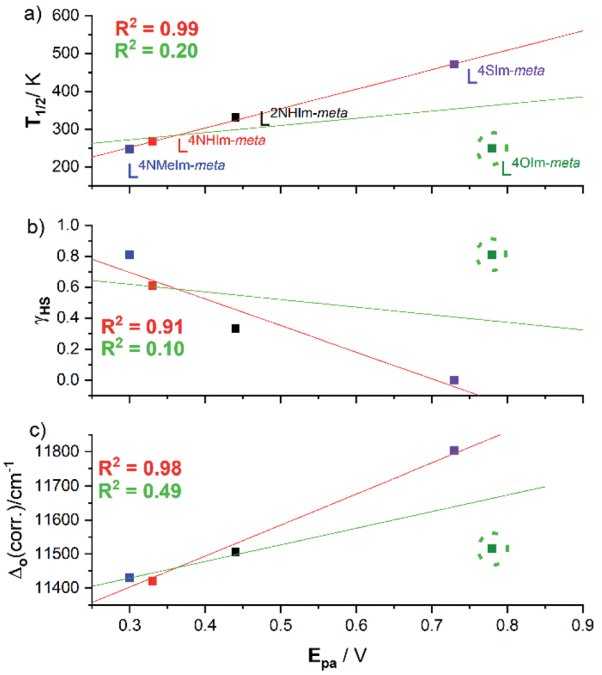

Fig. 12 (a) Strong correlations of oxidation potential (E_{pa}) for the four helicates that show reversible redox, **1**·4H$_2$O (black), **2**·6H$_2$O (red), **3**·5H$_2$O (blue) and **5**·2.5H$_2$O (purple), with (a) $T_{1/2}$ (R^2 = 0.99), (b) γ_{HS} (R^2 = 0.91), (c) $\Delta_{o(corr.)}$ (R^2 = 0.98). But please note that the 4-oxazole helicate with the irreversible redox event, [Fe$^{II}_2$(L$^{4OIm\text{-}meta}$)$_3$](BF$_4$)$_4$·6H$_2$O (**4**·6H$_2$O; green, lime circle), is a clear outlier in all three cases, so when it is included in the linear fit the R^2 drops to (a) 0.20, (b) 0.10 and (c) 0.49.

soluble in 0.1 M TBAPF$_6$. Four of the five complexes, **1**·4H$_2$O (E_m = 0.39 V), **2**·6H$_2$O (E_m = 0.27 V), **3**·5H$_2$O (E_m = 0.25 V) and **5**·2.5H$_2$O (E_m = 0.67 V), showed a reversible Fe(II)/Fe(III) redox process. In the case of the 4-oxazole helicate **4**·6H$_2$O, an irreversible oxidation event, at higher E_{pa} = 0.78 V than the others, was observed (Fig. 11).

The five helicates, identified by ligand, in order of decreasing E_{pa}, are as follows:

4·6H$_2$O (E_{pa} = 0.78 V) ~**5**·2.5H$_2$O (E_{pa} = 0.73 V) > **1**·4H$_2$O (E_{pa} = 0.44 V) > **2**·6H$_2$O (E_{pa} = 0.33 V) ~**3**·5H$_2$O (E_{pa} = 0.30 V)

In general, the presence of an electron donating group pushes more electron density onto a metal centre making it easier to oxidise, and *vice versa*. Therefore, the oxidation potential (E_{pa}) for 1-methyl-4-imidazole helicate **3**·5H$_2$O (0.30 V) is lower than 4-imidazole helicate **2**·6H$_2$O (0.33 V), which is attributed to the presence of the electron donating group –NMe in **3**·5H$_2$O, making the Fe(II) centre easier to oxidise.[36,82]

Correlations of SCO $T_{1/2}$ *versus* Δ_o *versus* E_{pa}

Interestingly, the four helicates with the reversible redox events, **1**·4H$_2$O, **2**·6H$_2$O, **3**·5H$_2$O and **5**·2.5H$_2$O, show a strong linear correlations between the (a) oxidation potential E_{pa} *vs.* the SCO $T_{1/2}$ (R^2 = 0.99, Fig. 12a, red line), and (b) γ_{HS} (298 K) *vs.* E_{pa} (R^2 = 0.91, Fig. 12b, red line). But when the helicate with the irreversible redox event, 4-oxazole helicate **4**·6H$_2$O, included in the linear fit the R^2 drops to just 0.20 (Fig. 12a, green line) and 0.10 (Fig. 12b, green line). Given the above, unsurprisingly there is also a strong linear correlation (R^2 = 0.98) of Δ_o and E_{pa} for the four reversible complexes (Fig. 12c, red line), which when **4**·6H$_2$O is included again drops, to R^2 = 0.49 (Fig. 12c, green line), *i.e.* in all cases the inclusion of the 4-oxazole helicate **4**·6H$_2$O which shows irreversible redox in these correlations leads to a big drop in R^2, to 0.10–0.49.

In summary, for the four complexes with reversible redox, E_{pa}(Fe$^{II/III}$) is strongly positively correlated with $T_{1/2}$ and Δ_o (R^2 = 0.91–0.99), and strongly negatively correlated with the γ_{HS} fraction at 298 K. This shows that as the ligand field (Δ_o) and hence fraction LS increases, it gets harder to oxidise, *i.e.* E_{pa}(Fe$^{II/III}$) increases (Fig. 12 and Table 2).

As noted in the introduction, studies of both redox and SCO across a family of complexes are not common.[24,30–33] In the 1980's, in a family of nine solution SCO-active Fe(III) complexes, Kadish and co-workers observed the same trend as is seen here, the lower the γ_{HS} the easier it was to reduce (higher $E_{1/2}$, Fig. S1.2, ESI†).[32,33] On the other hand, in 1975 Drago and co-workers[30] had studied a family of four solution SCO-active mononuclear Fe(II) complexes of hexadentate ligands varying in number of *ortho*-methyl groups present, and showed the opposite: the complexes with the highest γ_{HS}, rather than those with least electron-donating methyl groups (perhaps due to steric factors), were the most difficult to oxidise.[30] Simplistically, SCO $T_{1/2}$ values are expected to increase with increasing Δ_o whereas redox potentials $E_{1/2}$ are expected to increase with decreasing HOMO energy level. So the observation of some correlations between these two distinct properties is intriguing and warrants further attention. Hence a collaborative study

Table 2 Summary of cyclic voltammetry data obtained for dinuclear iron(II) helicates, **1–5**, in MeCN (0.1 mol L^{-1} TBAClO$_4$ unless indicated with * in which case, for solubility reasons, 0.1 M TBAPF$_6$ was used) *versus* 0.01 mol L^{-1} Ag/AgNO$_3$ at 200 mV s^{-1}, along with the $T_{1/2}$ and γ_{HS}(298 K) in MeCN solution, and the Δ_o for the nickel(II) analogues

Complexes	E_{pa} (V)	E_{pc} (V)	E_m (ΔE) (V)	$T_{1/2}$ (K)	γ_{HS} 298 K	Δ_o (cm^{-1}) (Ni$_2$L$_3$)
L$^{2NHIm\text{-}meta}$ (**1**·4H$_2$O)	0.44	0.34	0.39 (0.10)	331	0.33	11 505
L$^{4NHIm\text{-}meta}$ (**2**·6H$_2$O)	0.33	0.22	0.27 (0.11)	267	0.61	11 420
L$^{4NMeIm\text{-}meta}$ (**3**·5H$_2$O)	0.30	0.20	0.25 (0.10)	247	0.81	11 430
L$^{4OIm\text{-}meta}$ (**4**·6H$_2$O)	0.78	Irrev	Irrev	249	0.81	11 516
*L$^{4SIm\text{-}meta}$ (**5**·2.5H$_2$O)	0.73	0.61	0.67 (0.12)	471	0	11 804

probing this family of interesting helicates in detail, using a range of theoretical models, will be carried out in the future in order to better understand the basis of the correlations observed.

Conclusion

The previously reported ditopic **Rat** ligands consisted of a pair of pyrimidine-triazole pockets linked through *meta*-phenylene which resulted in Fe(II) dinuclear helicates that were trapped in the LS state.[57] So herein, the strong ligand field pyrimidines (azines) were replaced by lower ligand field azoles. Five such ligands have been prepared ($\mathbf{L}^{\mathbf{azole\text{-}}\mathit{meta}}$: $\mathbf{L}^{\mathbf{2NHIm\text{-}}\mathit{meta}}$, $\mathbf{L}^{\mathbf{4NHIm\text{-}}\mathit{meta}}$, $\mathbf{L}^{\mathbf{4NMeIm\text{-}}\mathit{meta}}$, $\mathbf{L}^{\mathbf{4OIm\text{-}}\mathit{meta}}$ and $\mathbf{L}^{\mathbf{4SIm\text{-}}\mathit{meta}}$) along with the corresponding triply bridged dinuclear helicates $[M^{II}_2L_3](BF_4)_4\cdot$solvents with M = Fe or Ni. Single crystal X-ray structures of the iron(II) helicates (**1–5**) confirmed that they are indeed helicates, and are in the [LS–LS] state at 100 K.

ESI-MS and ^{1}H DOSY NMR spectroscopy studies confirmed the robustness of **1–5** in MeCN solution. Indeed, a strong linear correlation ($R^2 = 0.98$) was seen between the diffusion coefficient and the molecular weight for the nine Fe_2L_3 helicates (**7**) and Fe_4L_6 cages (**2**) prepared to date,[57] regardless of the γ_{HS} at 298 K ranging from 0 to 0.81.

VT-NMR Evans method studies of **1–5** in CD_3CN solution (243–343 K) revealed that all of the complexes undergo incomplete SCO within this temperature range, with $T_{1/2}$ values ranging from 247 to 471 K. The SCO was also followed by VT-UV-vis spectroscopy (253–303 K) in CH_3CN solution, by monitoring changes in the absorbance of either the charge transfer band for **1**, or of the d–d band for **2–5**.

UV-vis spectra of the corresponding Ni(II) helicates revealed the ligand field splitting energy $\Delta_{o(corr.)}$ for four of the $\mathbf{L}^{\mathbf{azole\text{-}}\mathit{meta}}$ ligands falls in the range 11 420–11 516 cm^{-1} (azole = 2-imidazole, 4-imidazole, 1-methyl-4-imidazole and 4-oxazole) whereas the fifth ligand imposes a significantly stronger ligand field, 11 804 cm^{-1} (azole = 4-thiazole).

Cyclic voltammetry studies in acetonitrile solution showed a Fe(II)/Fe(III) redox process that was reversible for four of the helicates, but irreversible for the 4-oxazole helicate $\mathbf{4}\cdot 6H_2O$. For the four reversible cases, excellent linear correlations of: E_{pa} with $T_{1/2}$ ($R^2 = 0.99$), E_{pa} with γ_{HS} ($R^2 = 0.91$) and E_{pa} with $\Delta_{o(corr.)}$ ($R^2 = 0.98$) are observed.

This is a unique study, as it determines all three properties, ligand field splitting energy Δ_o, SCO $T_{1/2}$ and oxidation potential E_{pa} across a family of complexes – here for a family of five robust triply bridged dinuclear helicates differing in the choice of non-coordinated diazole heteroatom. In doing so it provides a rare illustration of the textbook statement that the stronger the ligand field ($\Delta_o\uparrow$) the more the LS state is stabilised over the HS state ($T_{1/2}\uparrow$; strong correlations, $R^2 > 0.87$). Also, less intuitively, a connection is made between the SCO and redox properties of this family of helicates: for the four reversible systems the stronger the ligand field ($\Delta_o\uparrow$) and higher the $T_{1/2}$ ($\uparrow$), the harder the Fe(II) helicate is to oxidise to Fe(III) ($E_{pa}\uparrow$). Future studies will include collaborative theoretical studies to probe these interesting helicates in more detail.

Author contributions

S. S. carried out all of the experimental work. S. B. conceived and supervised the project. S. S. prepared the first draft of the manuscript and S. B. and S. S. refined it to publication standards.

Conflicts of interest

There are no conflicts to declare.

Acknowledgements

We thank the University of Otago for supporting this work (including a doctoral scholarship and publishing bursary to SS), and Mr Ian Stewart (Otago) for measuring the ESI-MS and NMR spectra.

Notes and references

1 M. A. Halcrow, *Spin-Crossover Materials: Properties and Applications*, John Wiley & Sons, Ltd, Chichester, 1st edn, 2013.
2 P. Gütlich and H. A. Goodwin, Spin Crossover in Transition Metal Compounds I-III, *Top. Curr. Chem.*, 2004, **233-235**.
3 P. Gütlich, Y. Garcia and T. Woike, *Coord. Chem. Rev.*, 2001, **219–221**, 839–879.
4 J.-F. Létard, P. Guionneau and L. Goux-Capes, *Top. Curr. Chem.*, 2004, **235**, 221–249.
5 M. Mikolasek, M. D. Manrique-Juarez, H. J. Shepherd, K. Ridier, S. Rat, V. Shalabaeva, A.-C. Bas, I. E. Collings, F. Mathieu, J. Cacheux, T. Leichle, L. Nicu, W. Nicolazzi, L. Salmon, G. Molnár and A. Bousseksou, *J. Am. Chem. Soc.*, 2018, **140**, 8970–8979.
6 J.-M. Lehn, *Supramolecular chemistry: concepts and perspectives*, VCH, Weinheim, 1995.
7 E. C. Constable and A. M. W. Cargill Thompson, *J. Chem. Soc., Dalton Trans.*, 1994, 1409–1418.
8 A. Lennartson, P. Southon, N. F. Sciortino, C. J. Kepert, C. Frandsen, S. Mørup, S. Piligkos and C. J. McKenzie, *Chem.–Eur. J.*, 2015, **21**, 16066–16072.
9 F. Wang, C.-Y. Zhu, Y.-Q. Zhang, R.-Z. Liao, W. Xia, J.-C. Hu, J. Wu and H. Liu, *Dalton Trans.*, 2018, **47**, 13142–13150.
10 S. Rodríguez-Jiménez and S. Brooker, *Inorg. Chem.*, 2019, **58**, 8188–8197.
11 R. W. Hogue, S. Singh and S. Brooker, *Chem. Soc. Rev.*, 2018, **47**, 7303–7338 and inside front cover.
12 H. S. Scott, R. W. Staniland and P. E. Kruger, *Coord. Chem. Rev.*, 2018, **362**, 24–43.
13 A. J. McConnell, *Supramol. Chem.*, 2018, **30**, 858–868.
14 N. Struch, C. Bannwarth, T. K. Ronson, Y. Lorenz, B. Mienert, N. Wagner, M. Engeser, E. Bill, R. Puttreddy, K. Rissanen, J. Beck, S. Grimme, J. R. Nitschke and A. Lützen, *Angew. Chem., Int. Ed.*, 2017, **56**, 4930–4935.
15 R. A. Bilbeisi, S. Zarra, H. L. C. Feltham, G. N. L. Jameson, J. K. Clegg, S. Brooker and J. R. Nitschke, *Chem.–Eur. J.*, 2013, **19**, 8058–8062.

16 K. J. Howard-Smith, A. R. Craze, H. Zenno, J. Yagyu, S. Hayami and F. Li, *Chem. Commun.*, 2020, **56**, 8838–8841.
17 L. J. Charbonnière, A. F. Williams, C. Piguet, G. Bernardinelli and E. Rivara-Minten, *Chem.–Eur. J.*, 1998, **4**, 485–493.
18 F. Tuna, M. R. Lees, G. J. Clarkson and M. J. Hannon, *Chem.–Eur. J.*, 2004, **10**, 5737–5750.
19 L. Li, A. R. Craze, R. Akiyoshi, A. Tsukiashi, S. Hayami, O. Mustonen, M. M. Bhadbhade, S. Bhattacharyya, C. E. Marjo, Y. Wang, L. F. Lindoy, J. R. Aldrich-Wright and F. Li, *Dalton Trans.*, 2018, **47**, 2543–2548.
20 A. R. Craze, M. M. Bhadbhade, Y. Komatsumaru, C. E. Marjo, S. Hayami and F. Li, *Inorg. Chem.*, 2020, **59**, 1274–1283.
21 D. Pelleteret, R. Clérac, C. Mathonière, E. Harte, W. Schmitt and P. E. Kruger, *Chem. Commun.*, 2009, 221–223.
22 R. J. Archer, C. S. Hawes, G. N. L. Jameson, V. McKee, B. Moubaraki, N. F. Chilton, K. S. Murray, W. Schmitt and P. E. Kruger, *Dalton Trans.*, 2011, **40**, 12368–12373.
23 R. J. Archer, H. Scott, M. I. J. Polson, B. E. Williamson, C. Mathoniere, M. Rouzieres, R. Clerac and P. Kruger, *Dalton Trans.*, 2018, **47**, 7965–7974.
24 Y. Sunatsuki, R. Kawamoto, K. Fujita, H. Maruyama, T. Suzuki, H. Ishida, M. Kojima, S. Iijima and N. Matsumoto, *Inorg. Chem.*, 2009, **48**, 8784–8795.
25 S. Yukinari, M. Hisashi, F. Kunihiro, S. Takayoshi, K. Masaaki and M. Naohide, *Bull. Chem. Soc. Jpn.*, 2009, **82**, 1497–1505.
26 M. Darawsheh, L. A. Barrios, O. Roubeau, S. J. Teat and G. Aromí, *Chem.–Eur. J.*, 2016, **22**, 8635–8645.
27 W. R. Scheidt and C. A. Reed, *Chem. Rev.*, 1981, **81**, 543–555.
28 E. V. Dose, M. F. Tweedle, L. J. Wilson and N. Sutin, *J. Am. Chem. Soc.*, 1977, **99**, 3886–3888.
29 S. G. Sligar, *Biochemistry*, 1976, **15**, 5399–5406.
30 M. A. Hoselton, L. J. Wilson and R. S. Drago, *J. Am. Chem. Soc.*, 1975, **97**, 1722–1729.
31 T. Kuroda-Sowa, R. Isobe, N. Yamao, T. Fukumasu, T. Okubo and M. Maekawa, *Polyhedron*, 2017, **136**, 74–78.
32 K. M. Kadish, K. Das, D. Schaeper, C. L. Merrill, B. R. Welch and L. J. Wilson, *Inorg. Chem.*, 1980, **19**, 2816–2821.
33 T. Zhu, C. H. Su, D. Schaeper, B. K. Lemke, L. J. Wilson and K. M. Kadish, *Inorg. Chem.*, 1984, **23**, 4345–4349.
34 M. G. Cowan, J. Olguín, S. Narayanaswamy, J. L. Tallon and S. Brooker, *J. Am. Chem. Soc.*, 2012, **134**, 2892–2894 and front cover feature.
35 J. N. McPherson, R. W. Hogue, F. S. Akogun, L. Bondì, E. T. Luis, J. R. Price, A. L. Garden, S. Brooker and S. B. Colbran, *Inorg. Chem.*, 2019, **58**, 2218–2228.
36 T. Tanaka, Y. Sunatsuki and T. Suzuki, *Inorg. Chim. Acta*, 2020, **502**, 119373.
37 W. Linert, M. Enamullah, V. Gutmann and R. F. Jameson, *Monatsh. Chem.*, 1994, **125**, 661–670.
38 S. Rodríguez-Jiménez, M. Yang, I. Stewart, A. L. Garden and S. Brooker, *J. Am. Chem. Soc.*, 2017, **139**, 18392–18396.
39 L. J. Kershaw Cook, R. Kulmaczewski, R. Mohammed, S. Dudley, S. A. Barrett, M. A. Little, R. J. Deeth and M. A. Halcrow, *Angew. Chem., Int. Ed.*, 2016, **55**, 4327–4331.
40 M. Halcrow, *Crystals*, 2016, **6**, 58.
41 C. J. Johnson, G. G. Morgan and M. Albrecht, *J. Mater. Chem. C*, 2015, **3**, 7883–7889.
42 S. Sundaresan, J. A. Kitchen and S. Brooker, *Inorg. Chem. Front.*, 2020, **7**, 2050–2059.
43 S. Schlamp, P. Thoma and B. Weber, *Eur. J. Inorg. Chem.*, 2012, 2759–2768.
44 S. Rodríguez-Jiménez, A. S. Barltrop, N. G. White, H. L. C. Feltham and S. Brooker, *Inorg. Chem.*, 2018, **57**, 6266–6282.
45 R. Nowak, E. A. Prasetyanto, L. De Cola, B. Bojer, R. Siegel, J. Senker, E. Rossler and B. Weber, *Chem. Commun.*, 2017, **53**, 971–974.
46 J. G. Haasnoot, *Coord. Chem. Rev.*, 2000, **200–202**, 131–185.
47 J. A. Kitchen and S. Brooker, *Coord. Chem. Rev.*, 2008, **252**, 2072–2092.
48 H. L. C. Feltham, A. S. Barltrop and S. Brooker, *Coord. Chem. Rev.*, 2017, **344**, 26–53.
49 R. Kulmaczewski, J. Olguín, J. A. Kitchen, H. L. C. Feltham, G. N. L. Jameson, J. L. Tallon and S. Brooker, *J. Am. Chem. Soc.*, 2014, **136**, 878–881.
50 M. H. Klingele, B. Moubaraki, J. D. Cashion, K. S. Murray and S. Brooker, *Chem. Commun.*, 2005, 987–989 and front cover feature.
51 R. W. Hogue, H. L. C. Feltham, R. G. Miller and S. Brooker, *Inorg. Chem.*, 2016, **55**, 4152–4165.
52 C. F. Herold, L. M. Carrella and E. Rentschler, *Eur. J. Inorg. Chem.*, 2015, **2015**, 3632–3636.
53 C. Köhler and E. Rentschler, *Eur. J. Inorg. Chem.*, 2016, 1955–1960.
54 C. F. Herold, S. I. Shylin and E. Rentschler, *Inorg. Chem.*, 2016, **55**, 6414–6419.
55 F. Fürmeyer, L. M. Carrella, V. Ksenofontov, A. Möller and E. Rentschler, *Inorg. Chem.*, 2020, **59**, 2843–2852.
56 M. H. Klingele and S. Brooker, *Eur. J. Org. Chem.*, 2004, 3422–3434.
57 S. Singh, R. W. Hogue, H. L. C. Feltham and S. Brooker, *Dalton Trans.*, 2019, 15435–15444.
58 S. Singh and S. Brooker, *Inorg. Chem.*, 2020, **59**, 1265–1273.
59 A. Spek, *Acta Crystallogr., Sect. C: Cryst. Struct. Commun.*, 2015, **71**, 9–18.
60 A. Craze, N. Sciortino, M. Badbhade, C. Kepert, C. Marjo and F. Li, *Inorganics*, 2017, **5**, 62.
61 N. G. White, J. A. Kitchen and S. Brooker, *Eur. J. Inorg. Chem.*, 2009, **2009**, 1172–1180.
62 K. F. Morris and C. S. Johnson, *J. Am. Chem. Soc.*, 1993, **115**, 4291–4299.
63 K. F. Morris and C. S. Johnson, *J. Am. Chem. Soc.*, 1992, **114**, 3139–3141.
64 D. Fujita, Y. Ueda, S. Sato, N. Mizuno, T. Kumasaka and M. Fujita, *Nature*, 2016, **540**, 563–566.
65 K. Gu, J. Onorato, S. S. Xiao, C. K. Luscombe and Y.-L. Loo, *Chem. Mater.*, 2018, **30**, 570–576.
66 S. Vázquez-Leyva, L. Vallejo-Castillo, C. A. López-Morales, J. E. Herbert-Pucheta, L. G. Zepeda-Vallejo, M. Velasco-Velázquez, L. Pavón, S. M. Pérez-Tapia and E. Medina-Rivero, *Anal. Chem.*, 2019, **91**, 14392–14400.

67 P. S. Pregosin, P. G. A. Kumar and I. Fernández, *Chem. Rev.*, 2005, **105**, 2977–2998.
68 H. Takezawa, T. Murase, G. Resnati, P. Metrangolo and M. Fujita, *Angew. Chem., Int. Ed.*, 2015, **54**, 8411–8414.
69 D. Fujita, Y. Ueda, S. Sato, H. Yokoyama, N. Mizuno, T. Kumasaka and M. Fujita, *Chem*, 2016, **1**, 91–101.
70 Q. F. Sun, J. Iwasa, D. Ogawa, Y. Ishido, S. Sato, T. Ozeki, Y. Sei, K. Yamaguchi and M. Fujita, *Science*, 2010, **328**, 1144–1147.
71 M. Tominaga, K. Suzuki, M. Kawano, T. Kusukawa, T. Ozeki, S. Shakamoto, K. Yamaguchi and M. Fujita, *Angew. Chem., Int. Ed.*, 2004, **43**, 5621–5625.
72 S. Denis-Quanquin, F. Riobé, M.-A. Delsuc, O. Maury and N. Giraud, *Chem.–Eur. J.*, 2016, **22**, 18123–18131.
73 M. P. Crockett, H. Zhang, C. M. Thomas and J. A. Byers, *Chem. Commun.*, 2019, **55**, 14426–14429.
74 C. Bartual-Murgui, S. Vela, M. Darawsheh, R. Diego, S. J. Teat, O. Roubeau and G. Aromi, *Inorg. Chem. Front.*, 2017, **4**, 1374–1383.
75 B. Weber and F. A. Walker, *Inorg. Chem.*, 2007, **46**, 6794–6803.
76 O. Kahn, *Molecular Magnetism*, VCH Publishers Inc., New York, 1993.
77 L. A. Yatsunyk and F. A. Walker, *Inorg. Chem.*, 2004, **43**, 757–777.
78 D. F. Evans, *J. Chem. Soc.*, 1959, 2003–2005.
79 I. Nikovskiy, A. Polezhaev, V. Novikov, D. Aleshin, A. Pavlov, E. Saffiulina, R. Aysin, P. Dorovatovskii, L. Nodaraki, F. Tuna and Y. Nelyubina, *Chem.–Eur. J.*, 2020, **26**, 5629–5638.
80 F. A. Cotton, G. Wilkinson, C. A. Murillo and M. Bochmann, *Advanced Inorganic Chemistry*, John Wiley & Sons, Inc., New York, 6th edn, 1999.
81 S. M. Hart, J. C. A. Boeyens and R. D. Hancock, *Inorg. Chem.*, 1983, **22**, 982–986.
82 D. C. Ashley and E. Jakubikova, *Inorg. Chem.*, 2018, **57**, 9907–9917.